Evaluation of 3D image-treatment algorithms applied to optical-sectioning microscopy

Nathalie B. Vicente (nathalie.vicente@gmail.com)

Javier E. Diaz-Zamboni (javierdiaz@bioingenieria.edu.ar)

Javier F. Adur (jadur@bioingenieria.edu.ar)

Víctor H. Casco (vcasco@bioingenieria.edu.ar)

Microscopy Laboratory, School of Engineering – Bioengineering, National University of Entre Ríos (UNER). Ruta 11, Km. 10 (3101) Oro Verde, Entre Ríos, Argentina.

Abstract

Information extracted from biological specimens is inherently three-dimensional. Though it is sometimes hard to handle, three-dimensional (3D) data provides greater understanding of biological structures and events than its bi-dimensional (2D) projections. This explains why optical-sectioning techniques are currently being explored and enhanced. The main objective of the present work was to evaluate the relevance of image-treatment algorithms, which included preprocessing (such as image-averaging, background correction and normalization of intensities) and processing (deblurring and restoration deconvolution) methods. This was done by implementing a quantification algorithm based on the Laplacian and a bright-point detector. Algorithms were applied to a 3D cell-adhesion skin model, based upon a specimen commonly used by our research group. Results indicated that certain preprocessing methods are required to enhance the performance of processing algorithms, while others must not be applied in order to ensure an adequate and precise quantification.

Keywords: Optical sectioning, quantification, three-dimensional image preprocessing and processing.

Resumen

La información extraída de especimenes biológicos es inherentemente tridimensional. Los datos tridimensionales (3D) permiten un mejor entendimiento de las estructuras y los eventos biológicos, comparados con sus proyecciones bidimensionales (2D), aunque a veces son más difíciles de manejar. Esto explica porqué actualmente se están investigando y mejorando las técnicas de seccionamiento óptico. El principal objetivo del presente trabajo fue evaluar la relevancia de algoritmos de tratamiento de imágenes, los cuales incluyen métodos de preprocesamiento (tales como promediación de imágenes, corrección de *background* y normalización de intensidades) y procesamiento (desconvolución de desborroneo y de restauración). Esto se realizó mediante la implementación de un algoritmo de cuantificación basado en el Laplaciano y un detector de puntos brillantes. Los algoritmos se aplicaron a un modelo 3D de adhesión celular en piel, basado en un espécimen comúnmente utilizado por nuestro grupo de investigación. Los resultados indican que ciertos métodos de preprocesamiento son requeridos para mejorar el rendimiento de los algoritmos de procesamiento, mientras que otros no deben ser aplicados para asegurar una adecuada y precisa cuantificación.

Palabras clave: Seccionamiento óptico, cuantificación, preprocesamiento y procesamiento de imágenes tridimensionales.

1. INTRODUCTION

A 3D representation of an object can be obtained employing either physical-sectioning or optical-sectioning techniques [4]. The former uses a microtome to produce several thin slices of a given specimen which are viewed, imaged and treated separately. On the other hand, in the case of optical-sectioning techniques (which include confocal [6], two-photon [10] and digital deconvolution microscopy [15]), several different in-focus images may be taken from within a thick specimen (one which is thicker than 15 μm). By taking images at regular intervals, a stack of them is produced; 3D projection softwares use these images to visualize the complete specimen as a 3D object.

In digital deconvolution microscopy, each image acquired contains information of the in-focus plane as well as out-of-focus data and noise; this is why they appear blurred and/or distorted. Images must be preprocessed to reduce the impact of random fluctuations and to prepare them for the processing algorithms (digital deconvolution *per se*).

Commonly used preprocessing approaches include image-averaging, background correction and intensity normalization. In the image-averaging process [4][14] two or more pictures of the same focus plane are averaged in a pixel by pixel basis; this means analogous pixels from the images that will be averaged are added together and then divided by the total amount of pixels considered. This procedure diminishes the impact of random noise yet it increases the amount of photobleaching [3][17] to which the biological specimen is exposed. Alternatively, background correction [4][14] aims to eliminate unwanted background intensities; this may be done by thresholding or by background subtraction. In the former a threshold or pixel-intensity limit is determined; any pixel with an intensity level equal to or below the threshold will be assigned the value zero (no intensity). Instead, background subtraction is a technique in which a background image is subtracted pixel-wise from the raw image. Since these methods eliminate information, they must be used judiciously so as not to erase useful data, especially when dealing with quantification. Lastly, we must consider that the integrated intensity of each image taken at different focal depths in wide-field microscopy should be approximately the same, though the distribution of pixel-intensity may vary from one image to the next. This is theoretically true, though it does not always occur due to oscillations in the intensity of excitation light, fluctuations in the power supply or other reasons. Normalization of intensities per plane (which is one type of intensity normalization) attempts to solve this.

In order to apply digital deconvolution algorithms, a thorough understanding of the image formation process is needed. This is modeled by equation (1),

$$i(x,y,z) = o(x,y,z) \otimes PSF(x,y,z) \quad (1)$$

where (x,y,z) are spatial coordinates, $i(x,y,z)$ is the image stack which is formed by the 3D convolution (denoted by $\otimes$) of the original object $o(x,y,z)$ and the 3D Point Spread Function $PSF(x,y,z)$ [5]. The PSF represents the behavior of the optical arrangement since it is the system's response to a unitary impulse input [4]. Deconvolution algorithms are employed to estimate the solution of equation (1), that is to say, to estimate $o(x,y,z)$. There are basically two categories in which these may be classified: non-iterative (deblurring) and iterative (restoration) algorithms [18].

The former are fast and do not require a great amount of computer resources (RAM, processor speed, etc) but they eliminate useful information; the latter, on the contrary, take longer and require a greater amount of computer resources, yet they tend to restore the out-of-focus intensity-information contained in each image of the stack to its correct spatial position.

The main objective of this work is to evaluate the relevance of preprocessing and deconvolution algorithms applied to a 3D model under study, which is based on a specimen commonly used by our research group (*Bufo arenarum* embryos). The model consists on E-cadherin expression; this is a protein which forms adherens junctions that help hold similar skin cells together [12]. Even though E-cadherin is present all around the circumference of the cell, it is found in denser clusters where more than two cells meet. When this protein is immunolabeled with a fluorophore (such as FITC) [16], these clusters look brighter than the circumferential ring for it contains more molecules per unit of length; these are given the name of puncta (singular: punctum) [1][9].

In order to perform the mentioned evaluation, quantification of the distribution of E-cadherin was done with the aid of a Laplacian and a bright-point detector algorithm. The former emphasizes sharp changes in voxel (volume-element, the 3D equivalent of the 2D pixel) intensity, therefore detecting cell borders and puncta where E-cadherin was expressed. The Laplace operator is denoted by Δ or ∇^2 and it is applied to any function **f** as shown below,

$$\Delta \mathbf{f} = \nabla^2 \mathbf{f} = (\nabla \cdot \nabla)\mathbf{f} = \left(\frac{\partial^2}{\partial x^2} + \frac{\partial^2}{\partial y^2} + \frac{\partial^2}{\partial z^2} \right) \mathbf{f} \quad (2)$$

where **f** depends on *x*, *y* and *z*, so it may be written as f(*x,y,z*). When dealing with image stacks, a 3D Laplace kernel is convolved with the images.

2. MATERIALS AND METHODS

2.1 Hardware and Software

Digital images were obtained using an Olympus BX50 Upright microscope, equipped with a white-light source for transmitted microscopy and a mercury UV-lamp used for epi-fluorescence microscopy. Images were taken with a cooled monochromatic Apogee CCD camera of 14 bits of resolution, 768x512 pixel^2 sensor size, 9x9 μm^2 pixel size, mounted to the microscope by a mount C lens (0.5X).

A stepping motor (RS 440-436) attached to the fine adjustment knob of the microscope, moved the stage up and down. It could move in steps of multiples of 5 nm [2] and was controlled via parallel port by a personal computer with an Intel 486 (100 MHz) processor, 16 MB of RAM and 4 GB of hard-disc space. Another computer (Intel Pentium IV 1.4 MHz with 640 MB of RAM and 30 GB of hard-disc space) was used to process the images which were transferred through Ethernet.

The CCD camera and stepping motor were controlled by special software which also included deconvolution algorithms [7] and a 3D visualization interface; it was designed in Object Pascal language [8]. Optical sectioning was automatically done by this tool after loading some basic

parameters which included file name, image width and height, time of exposure, distance between in-focus planes and motor speed (which determined the stage speed). Images were saved in TIFF 8 bit format and stacks were visualized with the aid of an algorithm which enabled Maximum Intensity Projection (MIP), implemented in OpenGL.

2.2 Optical Sectioning

The work area was chosen using a low magnification lens and white light (transmitted) which does not excite the fluorophore and therefore prevents photobleaching. When switching to UV illumination, the micrometric screw was adjusted to focus using a 20X lens (NA 0.7), determining a 0.9 μm xy resolution and voxels of 0.9x0.9x1 μm^3. Then, the stage was moved upwards a distance equal to half the total depth of the future stack and the stepping motor was programmed to move it downwards in step of 1 μm. The final stack was made up of 16 slices of 128x128 $pixel^2$.

2.3 Image Preprocessing and Processing

Raw images were preprocessed to normalize intensities per plane (we will refer to these as second raw images). First, the integrated intensity of each plane was calculated by adding the intensity of the individual pixels of each plane. Then, the average integrated intensity value was determined. Finally, each pixel of every plane was multiplied by the average value obtained and divided by that plane's previous integrated intensity, therefore ensuring that each plane would have the same integrated intensity by the end of the process. Intensity normalization was the only preprocessing method employed because we intended to prevent information loss (such would be the case of background correction) and because we aimed to reduce photobleaching to a minimum, therefore discarding image-averaging (data not shown).

Both raw and second raw images were deconvolved with a constrained iterative method of deconvolution, using an experimental PSF [7]; the former will be referred to as raw deconvolved while the latter will be called "second deconvolved".

2.4 Quantification Algorithm

The Laplacian was used to detect high-frequencies in Fourier space, which correspond to edges and points in the images. It was applied using a 3x3x3 $pixel^3$ kernel with unit gain. Then, the bright-point detector algorithm was implemented in calculus software to evaluate voxel intensity in the following manner. A threshold or pixel-intensity limit was set; any pixel with intensity equal to or greater than the threshold was considered as a bright point and its spatial position was stored. Though the procedure is similar to background correction by thresholding, the concept behind it is entirely different. In this way, bright points were counted and their location was recorded.

2.5 Biological Specimens

Bufo arenarum embryos, stage 19 (Gosner, 1960), were treated to study the E-cadherin expression pattern following the classical protocols [11][13]. They were fixed in Carnoy, washed in PBS 1X at room temperature and then treated with Triton X-100 (SIGMA) 0.1% in PBS during 30 minutes at room temperature. They were then incubated in goat normal serum 1:20 for 35 minutes followed by the primary monoclonal anti-E-cadherin antibody (rat antibody; Transduction Laboratories, Lexintong USA) 1:50 at 37°C for 75 minutes. After incubation, embryos were washed in PBS 1X

and incubated with the secondary antibody (IgG-FITC, SIGMA) 1:64 at room temperature for 105 minutes and then washed again with PBS 1X; finally, they were mounted in Vectashield Mounting medium (Vector Laboratories) to prevent fluorescent decay.

2.6 Summarizing Flowchart

In order to facilitate the understanding of the experiments described in the next section, we have summarized all of the steps involved in the flowchart shown below.

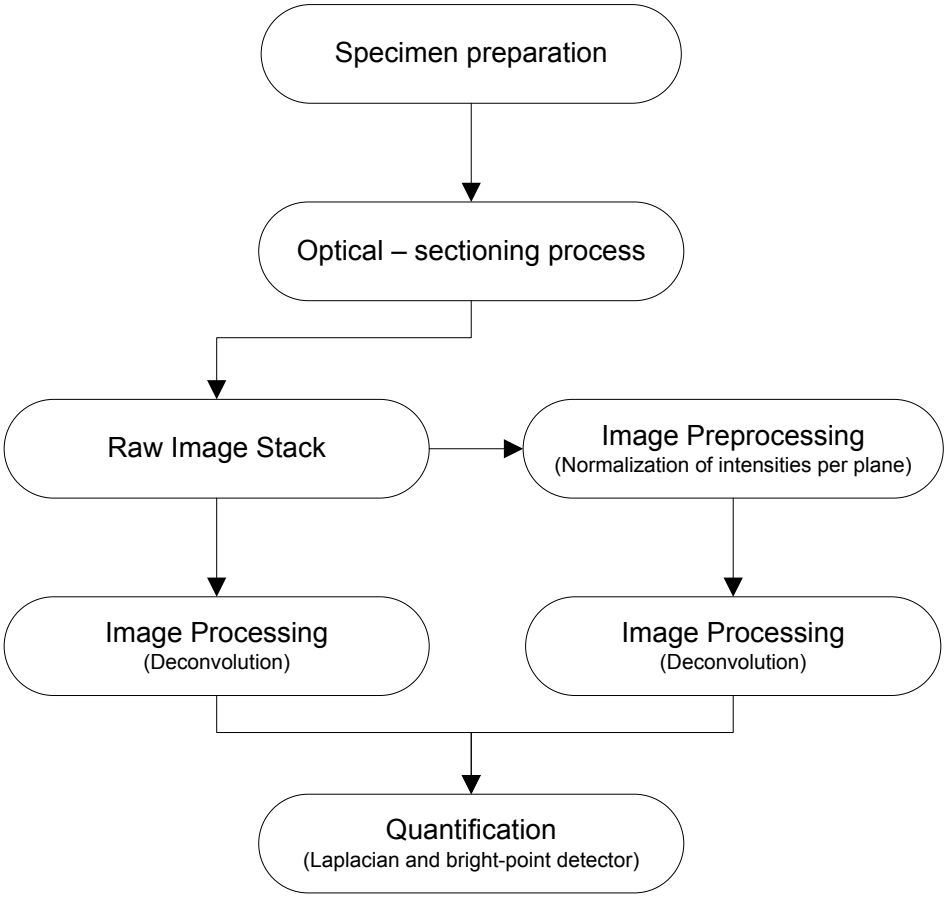

3. RESULTS

The experiment consisted of two different experiences. The first was carried out to compare preprocessed and processed images without the quantification algorithm, while the second employed the mentioned algorithm.

3.1 First Experience: Image Preprocessing and Processing Algorithms

Firstly, normalization of intensities per plane was evaluated. Figure 1 displays raw and second raw image stacks in two different views; the former look blurry and noisy compared to the latter in both projections. Secondly, deconvolution was analyzed; stacks which correspond to the deconvolution of the images presented in Figure 1 are shown in Figure 2. As described previously with non-deconvolved, raw deconvolved present more noise and have less definition than second deconvolved.

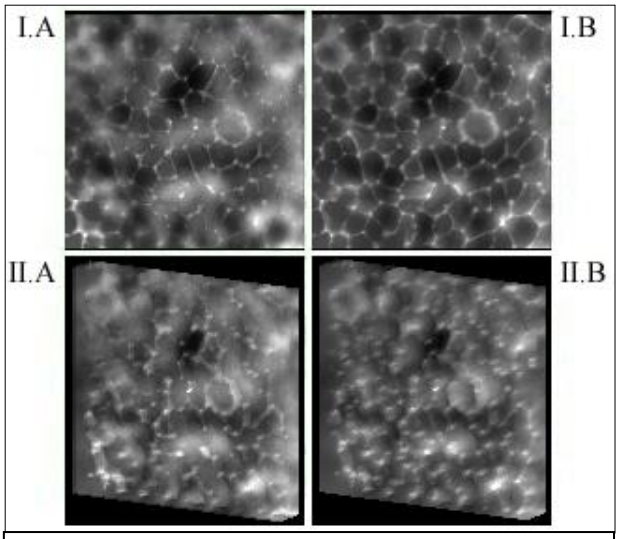

Figure 1 – *Comparison between non-deconvolved images before the Laplacian*. Left column (A): raw pictures. Right column (B): second raw (preprocessed) images. Top row (I): xy projection. Bottom row (II): tilted view.

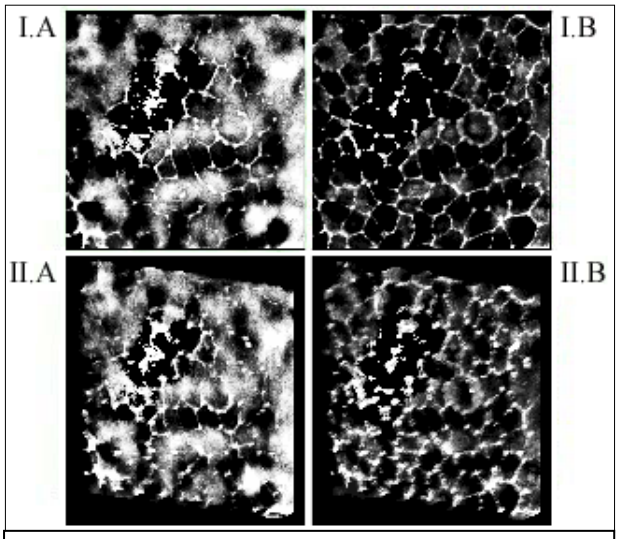

Figure 2 – *Comparison between deconvolved images before the Laplacian*. Left column (A): raw deconvolved pictures. Right column (B): second deconvolved images. Top row (I): xy projection. Bottom row (II): tilted view.

3.2 Second Experience: Quantification Algorithm

We used all sets of images mentioned earlier together with the Laplacian (to detect the presence of E-cadherin in the cell contour) and bright-point detector algorithms. Figure 3 and 4 show image stacks after the Laplacian was applied. The former shows saturated Laplacian raw stacks which have much more noise than Laplacian second raw images. Figure 4, instead, does not account for such a big difference between both sets of stacks. After applying the bright-point detector, a single image containing the location of bright points was selected from a stack; it is displayed, together with its analogues from each stack, in Figure 5 and 6. Four different threshold levels are shown,

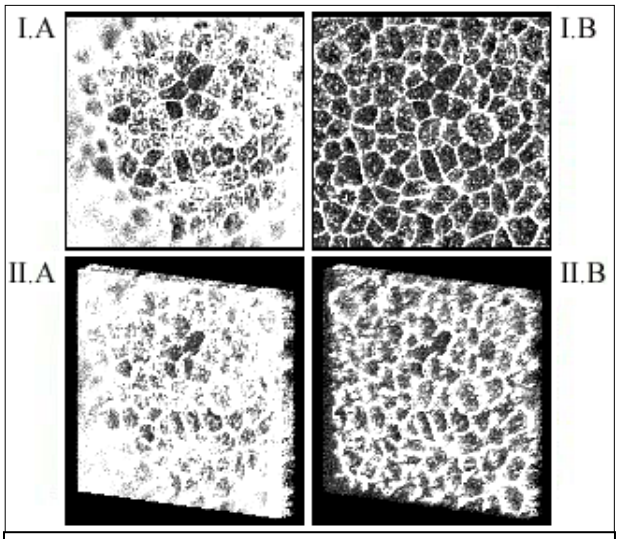

Figure 3 – *Comparison between non-deconvolved images after the Laplacian*. Left column (A): raw pictures. Right column (B): second raw (preprocessed) images. Top row (I): xy projection. Bottom row (II): tilted view.

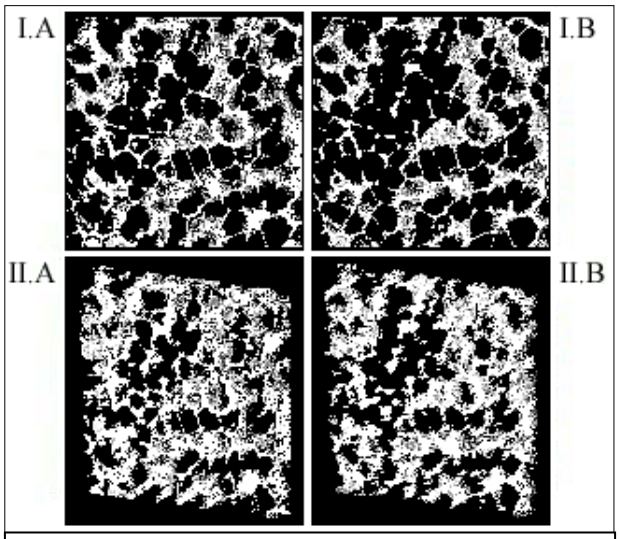

Figure 4 – *Comparison between deconvolved images after the Laplacian*. Left column (A): raw deconvolved pictures. Right column (B): second deconvolved images. Top row (I): xy projection. Bottom row (II): tilted view.

two for non-deconvolved images (raw and second raw) and two for deconvolved (raw deconvolved and second deconvolved). The total amount of bright points was calculated (see Table 1). The figures and table show that the amount of bright points detected increases as threshold levels decrease; furthermore, deconvolved stacks present a greater amount of these compared to their corresponding non-deconvolved pictures. The total amount of time needed to calculate the Laplacian kernel, apply it to an image stack, find bright points and store their spatial position is shown in Table 2.

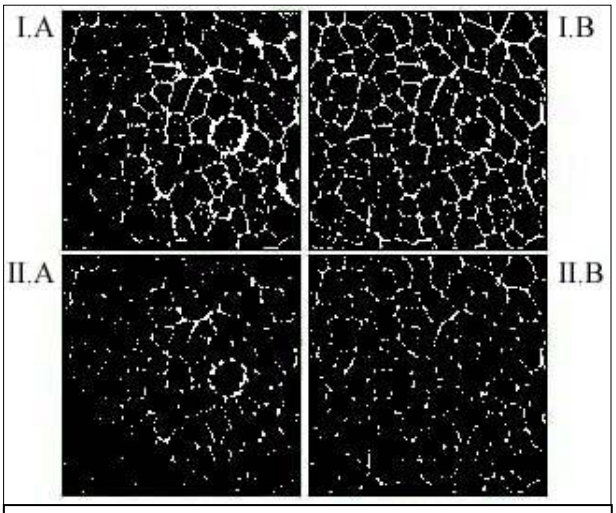

Figure 5 – *Bright points of a non-deconvolved image at different threshold levels*. Thresholds were set as a percentage of the maximum intensity level. Top row (I) and bottom row (II) show 35% and 40% thresholds, respectively. Left column (A): raw pictures. Right column (B): second raw (preprocessed) images.

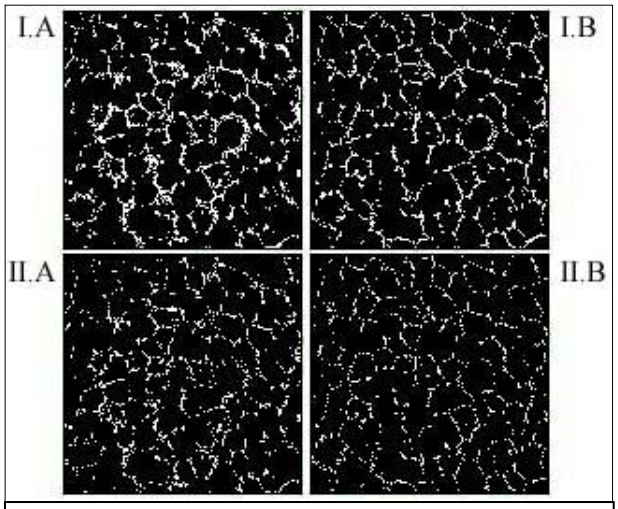

Figure 6 – *Bright points of a deconvolved image at different threshold levels*. Thresholds were set as a percentage of the maximum intensity level. Top row (I) and bottom row (II) show 80% and 85% thresholds, respectively. Left column (A): raw deconvolved pictures. Right column (B): second deconvolved images.

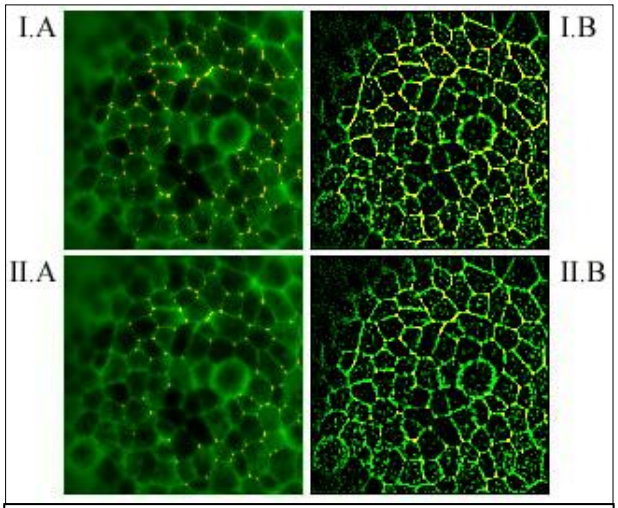

Figure 7 – *Co-localization of a non-deconvolved image*. Bright points were co-localized with raw pictures (left column, A) and second raw (preprocessed) images (right column, B). Different threshold levels are shown: 35% (top row, I) and 40% (bottom row, II) of maximum intensity.

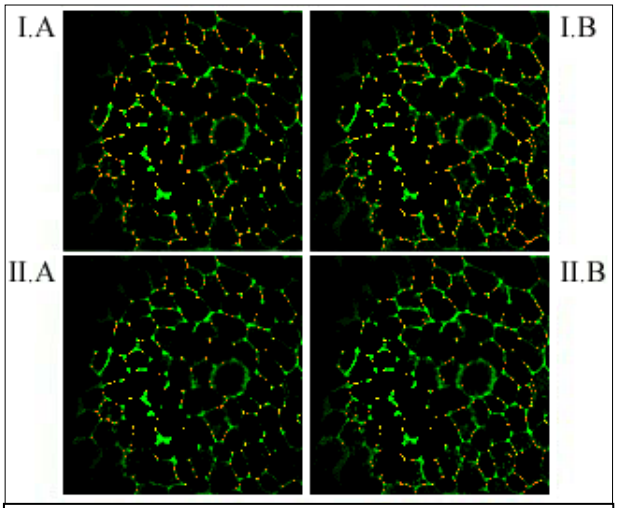

Figure 8 – *Co-localization of a deconvolved image*. Bright points were co-localized with raw deconvolved pictures (left column, A) and second deconvolved images (right column, B). Different threshold levels are shown: 80% (top row, I) and 85% (bottom row, II) of maximum intensity.

Additionally, images from Figure 5 and 6 were co-localized with their corresponding pictures before the Laplacian was applied (see Figure 7 and 8). The latter are shown in green while bright points are seen as red dots; when both are located in the same place, the pixel is colored in shades of yellow or orange (depending on the pixel intensity of the images before the Laplacian was applied).

Type of image stack	Total amount of bright points per threshold level			
	35 % of maximum	40 % of maximum	80 % of maximum	85 % of maximum
Raw	2716	914	3	3
Second raw	5564	1910	2	2
Raw deconvolved	255154	246651	2910	1665
Second deconvolved	252256	238263	2855	1499

Table 1 – *Amount of bright points at different threshold levels*.

Type of image stack	Time taken per threshold level (seconds)			
	35 % of maximum	40 % of maximum	80 % of maximum	85 % of maximum
Raw	0.6094	0.5469	0.6563	0.6406
Second raw	0.6250	0.6406	0.5313	0.7031
Raw deconvolved	1.0469	0.9688	0.6250	0.5625
Second deconvolved	0.8750	0.8594	0.5938	0.5469

Table 2 – *Time taken to calculate the Laplacian kernel, apply it to an image stack, find bright points and store their location, according to different threshold levels*.

4. DISCUSSION AND CONCLUSIONS

In the present work, normalization of intensities per plane was the only preprocessing algorithm employed for two main reasons: first, we did not want to eliminate information contained in the raw images (as would happen when using background correction) and second, we aimed to reduce photobleaching to a minimum (discarding image-averaging). This normalization process weights the integrated intensity of each plane relative to the corresponding mean integrated-intensity value; it therefore prevents sharp changes of intensity between successive planes which would saturate the Laplacian images (Figure 3, column A), thus interfering with quantification. Moreover, it favors the visualization of stacks since it improves contrast and definition (Figure 1 and 2).

Deblurring methods eliminate useful information, making the quantification process inaccurate. Consequently, we implemented a restoration algorithm which reassigns out-of-focus data to its correct spatial position; this is evidenced in Figure 2 since the haze of the non-deconvolved images is diminished. However, raw deconvolved stacks show saturated zones; this may be so because the deconvolution algorithm expects normalized images since the PSF presents this property (Figure 2, column A).

Considering the Laplace operator detects high frequencies, it is obvious that edges will be spot

together with unwanted noise. In Figure 3, the second raw stack does not account for the same amount of noise as the raw one does, which would indicate that the noisy appearance of the latter is due in part to factors beside random noise (such as variation of intensities between successive planes). This confirms that the Laplace operator must be applied to normalized stacks. On the other hand, in Figure 4, even though there are differences between raw deconvolved and second deconvolved, these are less significant than those between non-deconvolved stacks. Comparing the right columns of Figure 3 and 4, we might expect to obtain better results from second raw since those images look better. Nevertheless, this is not supported by the quantitative study.

The main hypothesis to consider when using the bright-point detector algorithm is that puncta can be modeled as bright spots. This may be regarded as a true statement because the FITC complex is smaller than the actual xy resolution and z resolution, which determine the dimensions of each voxel. Different threshold levels are shown in figures 5 through 8 with the purpose of ratifying the difference between non-deconvolved and deconvolved stacks in a threshold-independent manner. Deconvolved images present a greater amount of bright dots than the non-deconvolved do, at any given threshold value. This can be attributed to the fact that when deconvolution reassigns intensities, high-frequency zones are enhanced while low-frequency areas are depleted (process modulated by the PSF). Moreover, non-deconvolved bright points look more disperse than deconvolved bright dots and it is also more difficult to outline the cells when looking at non-deconvolved puncta (Figure 5 and 6).

Additionally, the co-localized representations (Figure 7 and 8) support the fact that puncta are located where more than two cells come together. These also confirm that puncta contain a denser population of E-cadherin than planes where two cells meet. Besides, it demonstrates that the application of the Laplacian may be used to spot edges and puncta (which correspond to high-frequencies in Fourier space), since bright points had the same location as the puncta. Based upon all the results shown above, the correct stack to work with when dealing with quantification is the second deconvolved one.

Another significant matter to take into account is the total amount of time taken to do all the procedures mentioned above; only the time taken to perform a fraction of these is presented in Table 2. Time is an important issue to consider, especially when dealing with many and/or large stacks. It is interesting to notice that it took about a second or less to calculate the Laplacian kernel, apply it to a set of images, find bright points and store their spatial position, using a 128x128x16 $pixel^3$ stack.

In conclusion, we demonstrated that knowledge about preprocessing and processing methods is important when dealing with quantification. Intensity normalization is an important preprocess since the deconvolution algorithm employed expects normalized stacks to perform optimally. Furthermore, deconvolved images ensure quantification will provide accurate and representative data.

REFERENCES

[1] Adams C.L., Chen Y.T., Smith S.J., Nelson W.J. Mechanisms of epithelial cell–cell adhesion and cell compaction revealed by high-resolution tracking of E-Cadherin–Green Fluorescent

Protein. *The Journal of Cell Biology*, vol. 142, nº 4, August 1998.

[2] Adur J., Schlegel J. Design, development and construction of an advance micrometric system for microscopes. *Bioengineering Degree Thesis*, Faculty of Engineering – Bioengineering. Entre Ríos National University. Argentina. November 1997.

[3] Benson D.M., Bryan J., Plant A.L., Gotto A.M., Smith L.C. Digital imaging fluorescence microscopy: spatial heterogeneity of photobleaching rate constants in individual cells. *The Journal of Cell Biology*, vol. 100, April 1985.

[4] Castleman K.R. *Digital Image Processing*. Prentice Hall, New Jersey, 1996.

[5] Cherniz A.S., Adur J., Deluca G.M., Casco V.H. Informática aplicada al desarrollo de un microscopia de seccionamiento óptico. *Simposio de informática y Salud, Anales JAIIO*, September 2002, ISSN 1666-1141.

[6] Conchello J.A., Lichtman J.W. Optical sectioning microscopy. *Nature Methods*, vol. 2, nº 12, December 2005.

[7] Diaz-Zamboni J., Adur J., Fiorucci M.P., Izaguirre F., Casco V.H. Algoritmo de desconvolución iterativo con restricción de positividad para imágenes de microscopía de fluorescencia tridimensional. *XV Congreso Argentino de Bioingeniería*, October 2005, ISBN 950-698-155-8.

[8] Diaz-Zamboni J. Software para usuarios de microscopía de desconvolución digital. *Bioengineering Degree Thesis*, Faculty of Engineering – Bioengineering, Entre Ríos National University, Argentina, September 2004.

[9] Gumbiner B.M. Cell adhesion: the molecular basis of tissue architecture and morphogenesis. *Cell*, vol. 84, February 1996.

[10] Helmchen F., Denk W. Deep tissue two-photon microscopy. *Nature Methods*, vol. 2, nº 12, December 2005.

[11] Izaguirre M.F., Adur J.F., Peralta-Soler A., Casco V.H. Induction of morphological alterations mediated by E-Cadherin and β-Catenin antibodies in Bufo Arenarum (Anura - Bufonidae). *Histology and Histopathology*, vol. 16, nº 4, October 2001.

[12] Lichtman J.W., Conchello J.A. Fluorescent microscopy. *Nature Methods*, vol. 2, nº 12, December 2005.

[13] Paz D.A., Alonso D.G., Pisano A., Casco V.H. Expression of isoforms of the neural cell adhesion molecule (NCAM) and polysialic acid during the development of the Bufo Arenarum olfactory system. *The International Journal of Developmental Biology*, vol. 39, nº 6, December 1995.

[14] Russ J.C. *The Image Processing Handbook*. CRC Press - IEEE Press, 1999.

[15] Sarder P., Nehorai A. Deconvolution methods for 3-D fluorescence microscopy images. *IEEE Signal Processing Magazine*, May 2006.

[16] Shaner N.C., Steinbach P.A, Tsien R. A guide to choosing fluorescent proteins. *Nature Methods*, vol. 2, nº 12, December 2005.

[17] Song L., Hennink E.J., Young T., Tanke H.J. Photobleaching kinetics of fluorescein in quantitative fluorescence microscopy. *Biophysical Journal*, vol. 68, June 1995.

[18] Wallace W., Schaefer L.H., Swedlow J.R. A workingperson's guide to deconvolution in light microscopy. *Biotechniques*, vol. 31, nº 5, November 2001.